

Simulation of the hydraulic fracturing process of fractured rocks by the discrete element method

Sousani Marina · Ingham Derek · Pourkashanian Mohamed · Sheng Yong · Eshiet Kenneth Imo-Imo

Received: 14 September 2014 / Accepted: 25 December 2014 / Published online: 9 January 2015
© Springer-Verlag Berlin Heidelberg 2015

Abstract This work presents a series of solid–fluid-coupled simulations of a natural fractured limestone sample. The aim of this paper is to investigate the effects of the fluid injection on its mechanical behaviour on the particle–scale. A detailed study of the influence of the fluid flow on the microstructure of the virtual model, including its internal stress state, the fracture initialization and propagation, and also the interactions between the existing fracturing networks and the new hydraulically induced fractures, has been performed. The results show that the change of the angle of the natural fracture alters the internal stress pattern of the model, concluding that for fractures between 15° and 45°, the stress regime below the fracture is always higher than the one related with the fractures between 45° and 90°. Furthermore, the propagation of cracks has also been affected by the fracture angle, where for fractures below 45°, the cracks tend to propagate downwards and travelling mostly as a group of cracks. In contrast, for fractures above 45°, easier upwards movement of the cracks and the formation of clusters that stray from the main volume of cracks are observed. The overall fracture growth is in agreement with what conventional theory generally states, where a hydraulic fracture is extended along the direction of the maximum compressive principal stress. However, the magnitude of this observation was restricted by the sample dimensions due to increased computational time for larger samples. Finally,

the relationship between the important cracking events (abrupt increases of microcracks) and the energy release within the model confirms the postulate that bond breakage causes further movement of particles and therefore increases the internal kinetic energy.

Keywords Hydraulic fracturing · Rocks · Induced fractures · Discrete element methodology (DEM) · Numerical modelling

Introduction

Hydraulic fracturing or fracking is a technique used in mining and involves the controlled cracking of the formation with the use of high-pressure liquid fluids. This process has been used for several decades in the oil and gas industry for enhanced oil recovery (EOR) and enhanced gas recovery (EGR), especially in the US, to extract more oil/gas through deep rock formations (Economides and Martin 2007; Kasza and Wilk 2012; Rahm 2011). Hydraulic fracturing is a combination of processes, such as the deformation of the formation due to an external mechanical load (i.e. pressure), the fluid flow through the induced cracks and the crack propagation (Adachi et al. 2007; Eshiet and Sheng 2010). While the technology behind these processes has been used for more than 30 years, underground formations constitute a complex system of variables (rock and well properties) that are not fully known and thus are still under investigation (Economides and Nolte 2000).

The application and benefits of hydraulic fracturing are far reaching. Although it is traditionally used for EOR and EGR practices, especially in unconventionally produced reservoirs, the concepts, accumulated experience and understanding of the phenomenon, can be readily applied

S. Marina · I. Derek · P. Mohamed
Energy Technology and Innovation Initiative (ETII),
University of Leeds, Leeds LS2 9JT, UK

S. Marina · S. Yong (✉) · E. K. Imo-Imo
School of Civil Engineering, University of Leeds,
Leeds LS2 9JT, UK
e-mail: y.sheng@leeds.ac.uk

in other operations. Geo-environmental problems are often associated with operations such as CO₂ sequestration (Eshiet and Sheng 2014a, b), underground coal gasification and the exploitation of thermal energy. One of the risks of CO₂ injection and storage is linked directly to uncontrolled build-up of injected and formation fluid pressures to levels that may cause underground movements, deformation and fracturing. These have several implications as suggested by geo-mechanical studies carried out to understand the impact in relation to the structure of geological formations (Eshiet and Sheng 2014a, b) and to assess the susceptibility of constructions surrounding the injection point (Eshiet and Sheng 2014b). Even in saline aquifers, which offer a considerable resource for long-term storage of CO₂, containment and injectivity, are subject to the suitability of reservoir characteristics (Tran Ngoc et al. 2014). Indiscriminate creation of fractures may ultimately result in the creation of pathways that could lead to the contamination of subsurface freshwater reserves. On the other hand, an aquifer permeability that is too low may attenuate the flow process despite being contained within the aquifer.

Extended research has been made in the past in order to analyse the hydraulic fracturing process with most of them involving the mechanical response of hydraulically pressurized intact rocks at the microscale (Eshiet et al. 2013; Eshiet and Sheng (2014b); Haimson 2004; Hamidi and Mortazavi 2014; Nagel et al. 2011; Shimizu et al. 2011; Sousani et al. 2014; Weng et al. 2011), shale–proppant interactions (Deng et al. 2014) or numerical experiments on large-scale jointed rock masses (Mas Ivars et al. 2011). However, the behaviour of natural fractured rocks, and more specifically the interaction between the existing and the new hydraulic fractures, which this work deals with, is in an early stage of development and thus constitutes an essential task. In this paper, a combination between the discrete element methodology (DEM) and the Lattice-Boltzmann method (Chen and Doolen 1998) based on the discretized version of the Navier–Stokes equations for porous media has been employed to build the solid part of the virtual limestone assembly and simulate the fluid flow. There are other techniques for simulating fluid flow in fractured masses in order to investigate the effect of high external mechanical load to groundwater flow and/or the simulation of pore pressure, both significant to ongoing operations (Wang et al. 2004; Wu et al. 2011). These include the computational fluid dynamics (CFD) and direct numerical simulation (Dong 2007; Moin and Mahesh 1998), the Continuum Medium approach (Zhu et al. 2014) and discrete fracture network and methods coupling both continuum and discrete media (Huang et al. 2014). However, each individual approach has its own limitations, such as restrictions on describing large-scale regions or partial production of detailed set of the geometrical parameters for individual fractures.

The DEM technique has been incorporated into PFC3D (particle flow code) (Itasca-Consulting-Group 2008c) based on particles that are connected by parallel bonds, replicating the cementation between grains in real rock formations. The technique allows the identification of systems at the microscale governing the fracture propagation, evaluates the influence of different rock matrixes on the hydraulic fracturing behaviour and provides further insight to the conductivity at the microscale. In order to build on the progress in modelling the macroscopic behaviour of the material, statistical assumptions on the interactions between the PFC particles, used to replicate the real rock, has to be considered. Nevertheless, accuracy can be achieved through a large number of particles but simulation efficiency is still a key limitation. Currently, software packages running on high-end personal computers used to perform DEM studies on fracture mechanics at the microscale are restricted at around 5×10^5 particles.

DEM theoretical background

PFC3D calculation cycle and stress distribution

The Discrete Element Methodology (DEM) is based on the generation of a virtual assembly of particles interacting with each other, and this is translated into a general contact law that is applied to the particles and their bonds. The two basic laws used repeatedly at every time step of the DEM calculations are Newton's second law for particles and a force–displacement law at the contacts. More specifically, Newton's second law is applied in order to calculate the motion of particles due to contact and the resulting body forces (updated velocities and locations), and the force–displacement law provides the updated contact forces derived from the relative displacements of particles at the contacts. Furthermore, Newton's second law is not applied for the walls as their movement is directly specified by the user, and thus, only the force–displacement law is applicable (Itasca-Consulting-Group 2008d).

Newton's law of motion between particles involves displacement, velocity and acceleration, whereas the rotational motion of the particles is described in terms of the angular velocity and angular acceleration. Furthermore, in PFC, the DEM analysis is a fully dynamic method and thus local damping, which acts on each ball, is necessary to dissipate kinetic energy. For any particle in translational motion, the equation of motion is given by

$$F_i + F_i^d = \begin{cases} m\ddot{x}_i, & \text{for } i = 1, 2, 3 \\ I\dot{\omega}_{(i-3)}, & \text{for } i = 4, 5, 6 \end{cases} \quad (1)$$

where F_i is the generalized force which includes the gravitational force, F_i^d is the damping force, m is the

particle’s mass, \ddot{x}_i is the particle’s translational acceleration, I is the moment of inertia, and $\dot{\omega}$ is the angular acceleration. The dots “.” on top of the variables denote derivatives with respect to time and the subscript “ i ”, is a free index that denotes the direction of the movement ($i = 1-3$ translational movements and 4–6 rotation).

Integrating the Eq. (1) yields the particle’s generalized velocity U_i given by

$$U_i = \begin{cases} \dot{x}_i & \text{for } i = 1, 2, 3 \\ \omega_{(i-3)} & \text{for } i = 4, 5, 6 \end{cases} \quad (2)$$

where \dot{x}_i and ω are the particle’s translational and angular velocities, respectively. The general equations describing the damping force is as follows:

$$F_i^d = -\alpha |F_i| \text{sign}(U_i) \quad (3)$$

where α is a non-dimensional frequency-independent damping constant with a default value of 0.7. From Eq. (3) it is obvious that only accelerating movement is damped, ensuring that no damping occurs in a steady-state motion.

A parallel bond can be translated as a set of elastic springs that are evenly distributed over a circular cross section in the contact plane and their centres at the contact point. Furthermore, they have a similar behaviour to a beam of length L as shown in Fig. 1b. For the case of two particles in contact with a parallel bond, they are assumed to be spheres in PFC3D. As shown in Fig. 1a, the action of particle A on particle B due to the parallel bond is as follows:

The force–displacement law relates the forces applied on the system with the particles’ mass and acceleration, an inertial damping coefficient necessary to dissipate kinetic energy, the resulting moment at each particle individually and at the system as a whole. The forces and moments are given by

$$F_i = F_i^n + F_i^s \quad (4)$$

$$M_i = M_i^n + M_i^s \quad (5)$$

where F_i , and M_i , are the total force and moment vectors and F_i^n , F_i^s , M_i^n , and M_i^s are the axial and shear components with respect to the contact plane, respectively. The subscript “ i ” is a free index that denotes the direction of the axis.

At the beginning of bond creation, the initial F_i and M_i are set to zero, but each relative displacement and rotation increment results in an increment in the values of elastic force and moment. These are added to the previous quantities, so that the total quantity at any time-step is given by

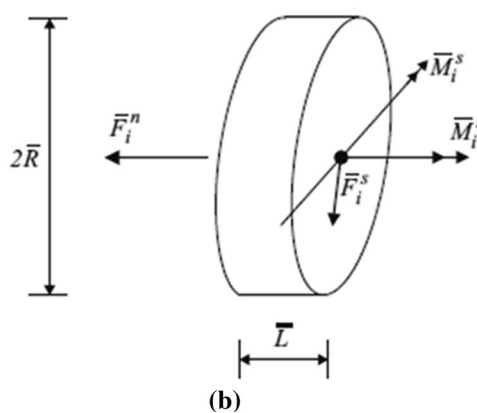
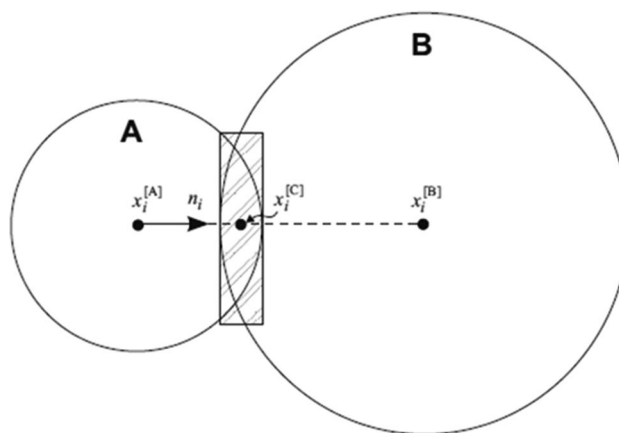


Fig. 1 Schematic of the **a** force between two particle spheres due to the presence of the parallel bond, and **b** parallel bond as a cylinder (Itasca-Consulting-Group 2008d)

$$\begin{aligned} F_i^n &= (F_i^n)_t + (\Delta F_i^n)_{t+1} \\ F_i^s &= (F_i^s)_t + (\Delta F_i^s)_{t+1} \\ M_i^n &= (M_i^n)_t + (\Delta M_i^n)_{t+1} \\ M_i^s &= (M_i^s)_t + (\Delta M_i^s)_{t+1} \end{aligned} \quad (6)$$

The increments of the elastic force, as well as the moment, are given as follows:

$$\begin{aligned} \Delta F_i^n &= (-k^n A \Delta U^n) n_i \\ \Delta F_i^s &= -k^s A \Delta U_i^s \\ \Delta M_i^n &= (-k^n J \Delta \theta^n) n_i \\ \Delta M_i^s &= -k^s I \Delta \theta_i^s \end{aligned} \quad (7)$$

with $\Delta U_i = V_i \Delta t$, and $\Delta \theta_i = (\omega_i^B - \omega_i^A) t$. where k^n, k^s are the normal and shear stiffnesses of the bond, respectively; V_i is the relevant motion at the contact; ΔU^n , ΔU_i^s are the normal and shear displacement overlaps, respectively; and A , J , and I are the area, polar moment of inertia and moment of inertia of the cross section of the bond, respectively. These sub-quantities are given by

$$\begin{aligned}
 k^n &= E_c/L \\
 k^s &= \frac{12IE_c}{AL^3} = \frac{3\pi R^4 E_c}{\pi R^2 L^3} \\
 V_i &= (\dot{x}_i)_B - (\dot{x}_i)_A \\
 A &= \pi R^2 \\
 I &= 1/4 \pi R^4 \\
 J &= 1/2 \pi R^4
 \end{aligned} \tag{8}$$

where E_c is the Young's modulus of the bond; \dot{x}_i is the translational velocity of the particles B and A, respectively; and ω_i is the rotational velocity of the particle. The distribution of the stress due to the parallel bonds and the interaction between the particles are calculated at every time-step. The maximum values of the tensile and shear stresses on the parallel bond perimeters are calculated using the general equation of stress following the beam theory:

$$\begin{aligned}
 \sigma_{\max} &= -\frac{F_i^n}{A} + \frac{M_i^s}{I} R \\
 \tau_{\max} &= \frac{|F_i^s|}{A} + \frac{|M_i^n|}{J} R
 \end{aligned} \tag{9}$$

Furthermore, stress is considered a continuum quantity and, hence, does not exist at every time-step in the PFC3D model because the model is discrete. The contact forces and displacements, attributed to the particle movement and used for the investigation of the mechanical behaviour of the model in the microscale, cannot be converted directly to a continuum model. They must follow a process of averaging its quantities in order to make the transition from the microscale to continuum. With the assumption that the stress is continuous and in equilibrium for each particle, the average stress in a measurement region can be expressed as follows:

$$\bar{\sigma}_{ij} = \left(1 - n / \sum_{N_p} V^{(p)} \right) \left(\sum_{N_p} \sum_{N_c^{(p)}} (x_i^{(c)} - x_i^{(p)}) F_j^{(c,p)} \right) \tag{10}$$

where $\bar{\sigma}_{ij}$ is the stress acting throughout the measurement region, n is the porosity and N_p is the number of particles in that region. $V^{(p)}$ is the volume of the particle (p), x_i is the location of a particle centroid and its contact, and F_j is the force acting on the particle p at contact c , respectively (Potyondy and Cundall 2004). The latter includes the normal and shear forces from Eq. (4) but neglects the parallel-bond moment.

Crack-growth theory

As already known, a microcrack in the PFC3D assembly is the subsequent bond breakage between two bonded particles. More specifically, each contact point develops a maximum tensile strength in the normal direction and

maximum shear contact-force strength due to the contact bond. Therefore, every time either the maximum tensile or shear force exceeds the tensile or shear strength ($\sigma_{\max} \geq \bar{\sigma}_{ij}$, $\tau_{\max} \geq \bar{\tau}$) of the spring (bond), then the parallel bond breaks. Thus, the number and the position of the possible microcracks are limited by the number and the position of the parallel bonds in the virtual assembly. In this work, the material demonstrates brittle behaviour under continuously increased load which is directly related to the presence of numerous microcracks propagated throughout the sample. The shift of this behaviour in a larger scale and hence, the transition from microcracks to macrocracks, with a continuously increased load, can describe the brittle behaviour of a real rock or reservoir.

There are in general two computational methods for modelling this behaviour: the indirect method, where the damage is represented through its effects on the constitutive relations (continuous mechanics) and the direct method, with the monitoring and tracking of the microcracks (Potyondy and Cundall 2004). In most indirect approaches, the material is considered to be continuous, and thus the relevant quantities of the material degradation are averaged in order to be used in fundamental relations and to characterize the microstructural damage (Krajcinovic 2000). In contrast, most direct approaches consider the material as a collection of structural units, such as springs and beams, or discrete particles bonded together at their contacts. Furthermore, they use the breakage of each structural unit or bond to characterize the damage (Schlangen and Garboczi 1997).

In the past, it was difficult to characterize problems with specific boundary conditions, such as the solution of a solid-boundary problem involving complicated deformation, using direct methods. Furthermore, these direct methods were used in order to study the general behaviour of the problem and develop complex relations that the indirect methods will use later to solve the problem. However, modern computers possess the required processing power to enable simulation of the entire problem bypassing the development of complex relations. Modelling the damage of a rock sample in PFC is such an example and falls into the category of the direct method. The interpretation of its mechanical behaviour is a complex procedure, due to extensive microcracking, and it is difficult to be described accurately with the use of continuum mechanics (Itasca-Consulting-Group 2008b).

Derivation of macroscopic parameters

Uniaxial and Brazilian tests

In the DEM logic, the macroscale properties of the sample cannot be directly described. They come as the result of the

interactions among the particles, and thus a micro-property process has to be set (Potyondy and Cundall 2004). A number of micro-properties are assigned between the particles and their contacts, and these in turn affect the resulting interactions. After the model has been fully developed, a fluid grid is set surrounding the sample in order to calculate the required quantities from each cell.

The calibration process is built upon a series of Uniaxial, Brazilian and single edge notch bending tests (SENB), using the 3D version of the PFC. The aim of these tests is to calibrate the virtual assembly in order to mimic the response of a generic real limestone rock by matching its uniaxial compressive strength (UCS), tensile strength, elastic properties (Young’s modulus E , and Poisson’s ratio ν) and the mode I fracture toughness (K_I) obtained from the literature (Hallsworth and Knox 1999; Knill et al. 1970; University-of-Stanford 2013) and the experimental work by Schmidt (1976) and Assane Oumarou et al. (2009). The general geo-mechanical properties of a limestone rock provide a wide range of values (Table 2), and the experimental work by Schmidt and Assane Oumarou delivers the linkage between the virtual model and actual experimental data. More specifically, part of Assane Oumarou’s work was to calculate the UCS and tensile strength on a number of cored Indiana LS limestone samples. According to his findings, the average UCS strength was 44 MPa, and the average tensile strength corresponded to the 1/9th of the average UCS strength (4.9 MPa). He also conducted a tensile strength sensitivity analysis concluding that the material’s tensile strength ranged between 3.1 and 6.2 MPa, validating his sample against the general geo-mechanical properties. Furthermore, part of Schmidt’s work on Indiana Limestone was to calculate its tensile strength and Young’s modulus on a number of specimens. It was estimated that the material’s tensile strength was ranging between 4.67 and 5.51 MPa, while its Young’s modulus ranged between 32.5 and 34.3GPa. The results showed that Indiana limestone, used from both researchers, lying well within the range provided from the literature, and therefore, their findings can be used for the calibration procedure. Both the Uniaxial and Brazilian tests have been discussed in detail by Sousani et al. (2014). Further, the complete set of input data used for the Uniaxial and Brazilian tests of the virtual assembly, named LIM1, is presented in Table 1.

A number of Uniaxial and Brazilian tests for the LIM1 assembly were repeated in order to confirm that the PFC results from each test do not deviate, and to evaluate the possible errors. The UCS and Brazilian results are considered accurate with an error of 0.14 %, lying within the wide range of limestone’s elastic constants and strength (compressive and tensile) provided in the literature (Table 2) and agreeing with the experimental results

Table 1 PFC micro-parameters used for the creation of the limestone sample (LIM1) and used in the Uniaxial and Brazilian simulated tests

	Uniaxial test	Brazilian test	
Geometry	Sample height (mm)	100	25
	Sample diameter (mm)	37.8	50
	Sample porosity (%)	15	15
	Gravity (m/s ²)	9.81	9.81
Particles	Ball minimum radius (mm)	0.85	0.85
	Ball radius ratio (R_{max}/R_{min})	1	1
	Radius multiplier	1.0	1.0
	Ball density (kg/m ³)	2,600	2,600
	Ball Young’s modulus (GPa)	30	30
	Ball stiffness ratio	1.0	1.0
	Ball friction	5.5°	5.5°
	Required isotropic stress (MPa)	0.4	0.4
Parallel bonds	Parallel-bond Young’s modulus (GPa)	20	20
	Parallel-bond normal/shear stiffness ratio (Pa/m)	1.4	1.4
	Parallel-bond normal strength (MPa)	30	30
	Std. deviation of normal strength	30×10^4	30×10^4
	Parallel-bond shear strength (MPa)	39	39
	Std. deviation of shear strength	30×10^4	30×10^4

Table 2 Typical geo-mechanical properties of limestone, according to the literature and test results obtained from the Uniaxial and Brazilian tests (Hallsworth and Knox 1999; Knill et al. 1970; University-of-Stanford)

Literature	Uniaxial and Brazilian test results	
UCS strength (MPa)	$q = 30\text{--}250$	$q = 54.8$ measurement-based $q = 45$ wall-based
Young’s modulus (GPa)	$E = 15\text{--}55$	$E = 34$
Poisson’s ratio	$\nu = 0.18\text{--}0.33$	$\nu = 0.21$
Tensile strength (MPa)	$\sigma_t = 5\text{--}25$	$\sigma_t = 9.7$

obtained by the aforementioned researchers. The results obtained from the simulated tests were monitored and recorded by two different measurement schemes: wall-based (corrected) and measurement-based methods (Itasca-Consulting-Group 2008b). The difference between the two methods is that in the wall-based scheme, the results are derived from measurements at each ball–wall contact point, where the effect of possible ball–wall overlap has been removed, whereas the measurement-based quantities are derived from three measurement spheres located in the upper, central and lower portions of the specimen. In terms

of calibration, even though the measurement-based scheme provides a more uniform averaged response over the entire specimen, it results into larger stresses and smaller strains compared with the wall-based scheme. Thus, it was considered best for this thesis to calibrate the virtual sample first by matching the results from the wall-based scheme with the ones from the literature, and second by using the measurement-based scheme to obtain the actual properties of the virtual sample.

Furthermore, the sample showed the expected behaviour in terms of stress versus strain. Figure 2a illustrates the typical curves from both schemes (wall-based and measurement-based) characterizing a rigid material that undergoes an abrupt failure. In the first region of Fig. 2a, the strength increases linearly with strain, and this corresponds to a recoverable (elastic) deformation, whereas the second region corresponds to total collapse and non-reversible changes of its shape. The maximum uniaxial compressive strength of the sample is 54.8 MPa based on the measurement-based scheme. Similar behaviour of almost linear increase of the strength versus strain was also observed during the Brazilian tensile test (Fig. 2b) with a maximum strength of about 10 MPa and a sudden decrease which results in failure.

Single edge notch bending (SENB) test

In the simulated three-point bending test, a rectangular specimen of dimensions $115 \times 25 \times 12.5$ mm (Fig. 3) was generated by a standard sample genesis procedure including (i) generation and compaction of the particles; (ii) set-up of the isotropic stress to provide internal

equilibrium; (iii) adjustment of particle sizes to reach at least three contacts with the neighbouring particles and elimination of those which do not follow the rule; and, (iv) finalization of the assembly. During this process, the virtual model consisting of particles and parallel bonds (cementation) was produced in the specified vessel. A notch has been created at the centre of the bottom part of the assembly by deleting the particles contained in the notched region. The size of both the virtual assembly and the notch were chosen according to Schmidt's work (Schmidt 1976) and the standard test method (ASTM) E1820-01-recommended specifications (ASTM 2001). More specifically, the size that could provide more accurate results of the fracture toughness was shown to coincide with the ASTM for the measurement of fracture toughness for metal alloys.

The procedure was similar to the uniaxial test, where frictionless walls in the x, y and z directions surround the vessel, forming an isotropic and well-connected virtual assembly. Next, all the walls were removed, and the model was cycled in order to absorb any residual forces caused by the lateral walls. Two fixed circular walls of high stiffness were set on the bottom ends of the virtual assembly, in order to provide the basic support (Fig. 3). Their radius was 3.1 mm, and the span between the supports was 100 mm, both following the ASTM E1820 guidelines ($R_{\min} = W/8$ and $S = 4 \times W$). The loading platen in this case was represented by four well-connected particles with strong contact bonds in order to act as a single unit (Fig. 3). Their stiffness was much higher than the average particle's stiffness, considering their role as a loading platen, and they were set just above the top surface of the assembly moving towards the top surface.

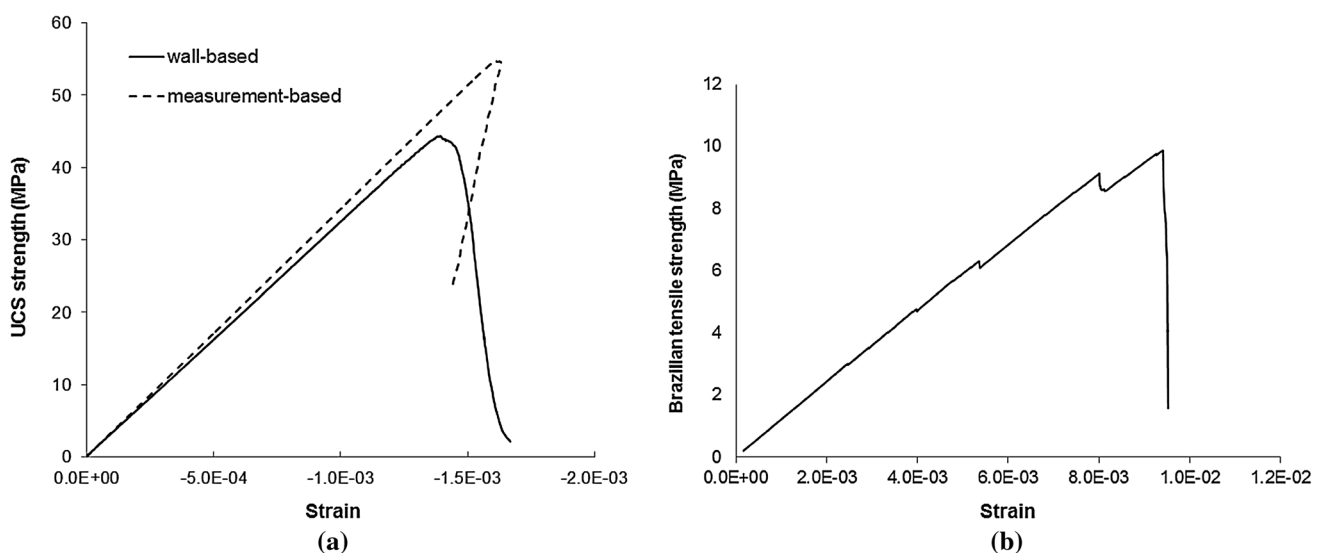


Fig. 2 The PFC3D output of the stress versus strain for the **a** LIM1 limestone assembly used in the simulated Uniaxial test utilising both the wall-based and measurement-based schemes, and **b** for the LIM1 limestone assembly used in the simulated Brazilian test

Fig. 3 Dimensions of the virtual LIM1 assembly for the single edge notch bending (SENB) test

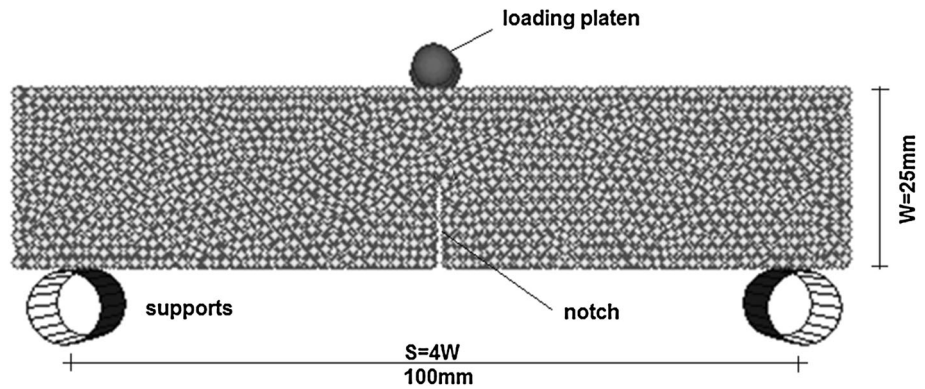


Table 3 Dimensions of the virtual LIM1 assembly and notched region for the single edge notch bending test

Input data		
Sample dimensions	Length (mm)	115
	Width (mm)	25
	Depth (mm)	12.5
Notch dimensions	Length <i>a</i> (mm)	12.5
	Width <i>W</i> (mm)	1.7
	Depth (mm)	12.5
Supports	Diameter (mm)	5
	Stiffness (GPa/m)	50
Loading platen	Diameter (mm)	3.1
	Stiffness (GPa/m)	200
	Density (kg/cm ³)	7,800
	Normal strength (GPa)	80
	Shear strength (GPa)	80

The complete set of input data used for the SENB test is summarized in Table 3.

The test was performed with a vertical platen velocity of $u_p = 0.01$ m/s, and the mode *I* stress intensity factor was continuously monitored until the failure of the sample, and the measurement of the fracture toughness follows the equation given by the ASTM Designation E1820-01:

$$K_I = \left[\frac{PS}{(BB_N)^{\frac{1}{2}}W^{\frac{3}{2}}} \right] f(a/W) \tag{11}$$

where

$$f(a/W) = \frac{3(a/W)^{1/2} \left[1.99 - (a/W)(1 - a/W) \times \left(2.15 - 3.93 \left(\frac{a}{W} \right) + 2.7(a/W)^2 \right) \right]}{2 \left(1 + \frac{2a}{W} \right) (1 - a/W)^{3/2}} \tag{12}$$

in which K_I is the mode *I* stress intensity factor; and *P* and *S* are the loads to failure and the span, respectively. Finally, *a*, B_N , *W* and *B* are the length of the notch, the depth of the notch, and the width and the depth of the sample, respectively.

The loading process was terminated when the required termination criterion was reached. More specifically, the stress intensity factor (K_I) was continuously monitored, increasing to a maximum value and then decreasing as the sample fails. Its maximum value ($K_{I_{max}}$) was recorded, and the test was terminated when the current value of the stress intensity factor became less than 0.3 times the previously recorded maximum value ($K_I < \alpha \times K_{I_{max}}$). Preliminary tests showed that this ratio was considered to be sufficient for the sample to reach its maximum fracture toughness, and a drop of more than 30 % in the value of the stress intensity factor indicated a failure of the sample and thus, this condition was used as a termination criterion. Figure 4a demonstrates the progress of the test at intervals, whereas Fig. 4b shows the profile of the stress intensity factor versus the opening of the notch and the maximum fracture toughness of the material.

According to the plot, the material’s resistance towards fracture is gradually increasing, reaching the maximum value of fracture toughness at $0.670 \text{ MPa}\sqrt{\text{m}}$, followed by a sharp decrease. The relatively low value of the fracture toughness of the material and the layout of the stress intensity factor indicate that the material undergoes brittle failure (Hertzberg 1996).

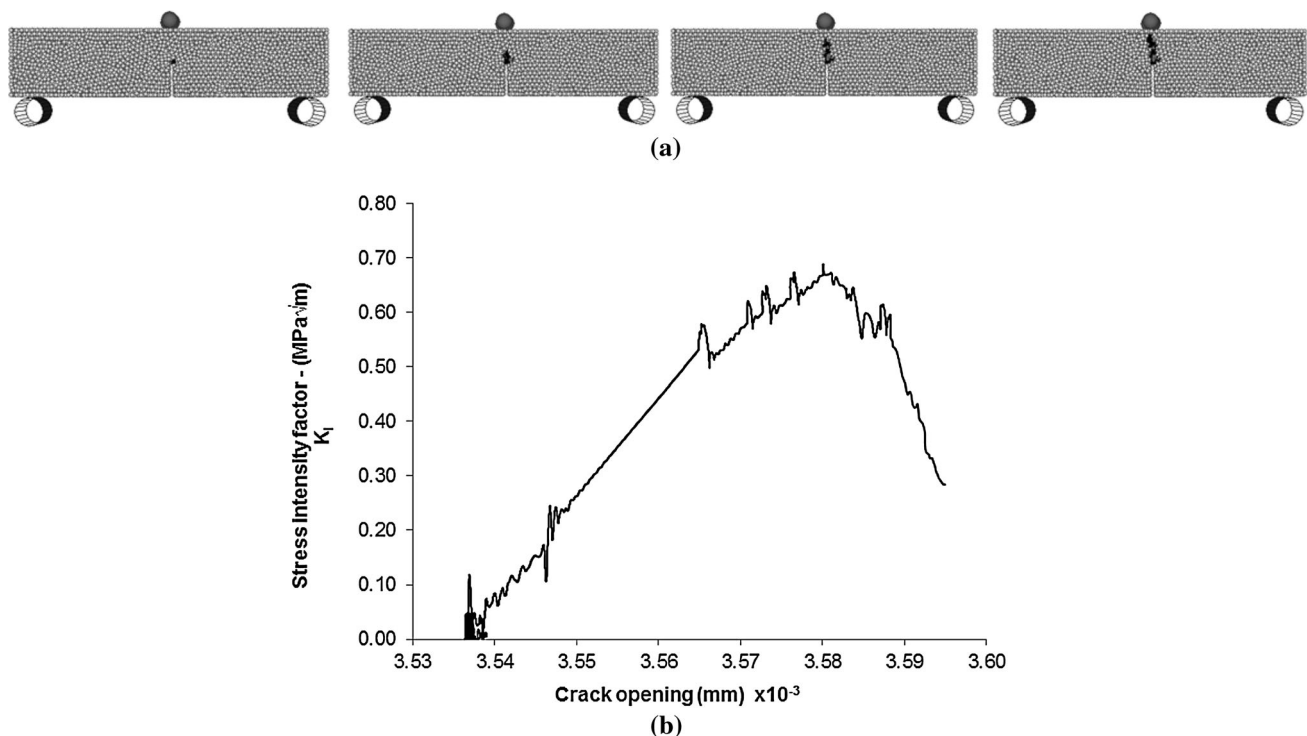


Fig. 4 **a** Progressive damage of the assembly resulting to microcracks at the tip of the notch and towards the top surface of the sample, **b** stress intensity factor versus crack opening, maximum value of fracture toughness $0.67 \text{ MPa}\sqrt{\text{m}}$

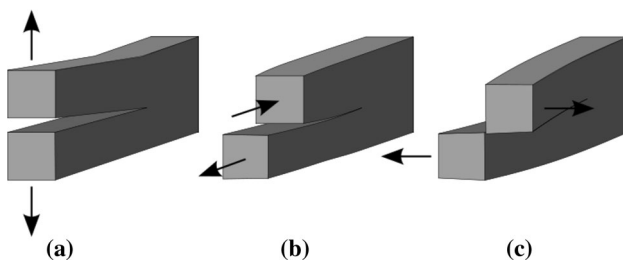


Fig. 5 The three types of fracture toughness modes: **a** Mode I normal to the crack plane, **b** Mode II in-plane shear that tends to slide the faces of the crack, and **c** Mode III out-of-plane shear (Anderson 1991)

Fracture mechanics in DEM

The presence of faults in rocks can contribute towards the escalation of any applied load as a result of the relationship between the surrounding loads, the geometry of the faults and the mechanical properties of the porous medium (Griffith 1921). Relations that relate the above parameters are defined in terms of the stress intensity factors. In linear fracture mechanics (LEFM), there are three different types of loading that a crack can experience due to external forces on the material as illustrated in Fig. 5. The most common type of loading for rocks is the Mode I (Schmidt 1976; Schmidt and Huddle 1977), where the principal load is applied in a normal direction with respect to the crack plane and tends to open the faces of the crack.

The SENB test was performed for five limestone samples of different UCS strength, named LIM1 to LIM5. The microparameters that control the elasticity of the samples remained constant, whereas the normal and shear strengths of the parallel bonds were altered. The ratio on the shear to normal strength was chosen to be 1.3 based on the experimental work of Assane Oumarou et al. (2009) for five different samples of Indiana limestone. According to their findings, the normalized stress ratio was mainly between 0.5 and 2.0, and therefore, it was considered best to take the average value of 1.3. The purpose of this test was to validate the simulated fracture toughness results with the ones obtained from the limited existing literature and relate the simulated SENB test with the LEFM. The test results showed that the fracture toughness of the PFC limestone assemblies are in excellent agreement with those in the work of Schmidt (1976), which gives results between $0.658 \text{ MPa}\sqrt{\text{m}}$ and $0.994 \text{ MPa}\sqrt{\text{m}}$ for 18 limestone samples, thus emulating the actual laboratory macroscale measurement technique for fracture toughness. Table 4 shows the values of the normal and shear strengths of the parallel bonds for each PFC sample, as well as the Uniaxial and the SENB test results. It can be observed that the values from the SENB test are in excellent agreement with the experimental values provided in the work of Schmidt.

Table 4 Input parameters of the normal and shear bond strengths for the conduction of the UCS and SENB tests, and the results obtained by the Uniaxial and Single Edge Notch Bending tests

	LIM1	LIM2	LIM3	LIM4	LIM5
Parallel-bond normal strength (MPa)	30	35	40	45	50
Parallel-bond shear strength (MPa)	39	45.5	52	58.5	65
UCS test results (MPa)	50	60	68	77	86
SENB test results (MPa√m)	0.670	0.790	0.910	0.990	1.030

It is important to point out that in DEM, a PFC particle must not be correlated with a real rock grain (Itasca-Consulting-Group 2008c). This is due to the fact that the virtual assembly is a precise microstructural sample and should not be confused with the microstructure of a rock. The particles in the PFC are used only as a means to quantize space and provide a comprehensive description of the model’s mechanical behaviour in terms of breakage of bonds (Itasca-Consulting-Group 2008a). For these reasons and the fact that DEM analysis is based on the discontinuity of the model (due to fractures), it cannot be directly compared with LEFM techniques. However, with the assumption that the individual microcracks in DEM are connected as part of the propagation process of a macroscopic fracture, the simulation results can be interpreted by LEFM. Several researchers have worked on this area relating the measurements of fracture strength from DEM

with those from LEFM (Huang et al. 2013; Moon et al. 2007; Potyondy and Cundall 2004). The work of Potyondy and Cundall (2004) related the LEFM to the bonded-particle model for a synthetic rock. More specifically, they translated the mode I fracture toughness of an infinite plate with a horizontal crack subjected to a remote tensile stress (Fig. 6a), to the following suggested formula for a parallel-bonded material:

$$K_I = \beta\sigma'_t\sqrt{\pi\alpha R} \tag{13}$$

where K_I is the mode I fracture toughness; α, β are non-dimensional constants with $\alpha \geq 1$ and $\beta < 1$; σ'_t is the normal strength of the parallel bond; and R is the radius of the particles. Furthermore, LEFM calculates the mode I fracture toughness of an infinite plate with a inclined crack subjected to a remote tensile stress (see Fig. 6(b)), given by:

$$K_I = \sigma_{y'y'}\sqrt{\pi L} = \sigma\cos^2(\varphi)\sqrt{\pi L} \tag{14}$$

The LIM1 sample has an induced crack at an angle $\varphi = 30^\circ$ (see Sect. 5), and therefore based on the work of Potyondy and Cundall (2004), Eq. (13) must be converted into the following formula:

$$K_I = [\beta\sigma'_t\sqrt{\pi\alpha R}] \cos^2(\varphi) \tag{15}$$

In this study, the total effects of the parameters α, β were merged into a single correlation factor μ that bridges the domain between the DEM and the LFM, given by

$$K_I = \mu\sigma'_t\sqrt{\pi R} \tag{16}$$

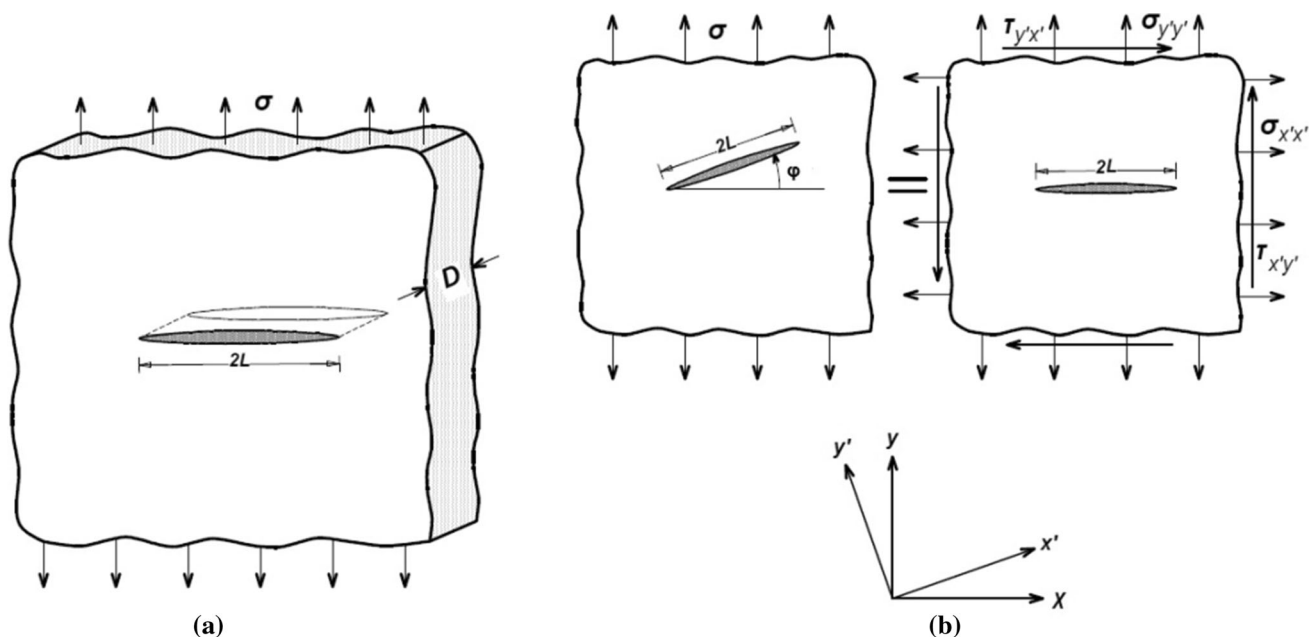


Fig. 6 **a** Infinite plate (width $\gg 2\alpha$) with a horizontal crack subjected to a remote tensile stress— $K_I = \sigma\sqrt{\pi L}$, and **b** infinite plate with a inclined crack subjected to a tensile stress that is not perpendicular to the crack plane— $K_I = \sigma_{y'y'}\sqrt{\pi L} = \sigma\cos^2(\varphi)\sqrt{\pi L}$ (Anderson 1991)

More specifically, the factor μ is used to determine the fracture toughness value from Eq. (15). Combining the values of the fracture toughness obtained from the SENB test for the samples LIM1 to LIM5 with Eq. (16), we obtain a relationship between μ and K_I which gives an approximate solution:

$$\mu = -5 \times 10^{-18} K_I^3 + 10^{-11} K_I^2 - 9 \times 10^{-6} K_I + 2.8532 \tag{17}$$

The next research steps include generating more samples in order to produce a more accurate version of Eq. (17), which describes the relationship between the fracture toughness of a material and the DEM correlation factor more efficiently. Using this method, and combining the SENB test and Eqs. (15) and (16), we can relate the results from the SENB test with the fracture toughness based on the DEM approach. More specifically, inserting

the values of the fracture toughness from the SENB test into Eq. (16), we can obtain the values for μ . Furthermore, inserting these values in Eq. (15), the values of fracture toughness based on the DEM approach are derived.

Simulation of the hydraulic fracturing process

The LIM1 sample was considered for the hydraulic fracturing test, with a DEM fracture toughness of $0.262 \text{ MPa}\sqrt{\text{m}}$. This value was obtained from the aforementioned method, and it can be observed that is in good agreement with the SENB fracture toughness ($0.660 \text{ MPa}\sqrt{\text{m}}$) of the material. The virtual assembly had dimensions 60-mm length, 40-mm width and 40-mm depth. Although there are no guidelines, the dimensions were carefully chosen so that the sample would be large enough to enhance the fracking process while also being efficient in terms of simulation. It comprised 31540 particles of uniform

Fig. 7 Schematics of (a) the geometry of the induced fracture of the LIM1 assembly under the angle of 30° , and (b) the geometry of all the induced cracks under the angle of $30^\circ, 45^\circ, 60^\circ$ and 90°

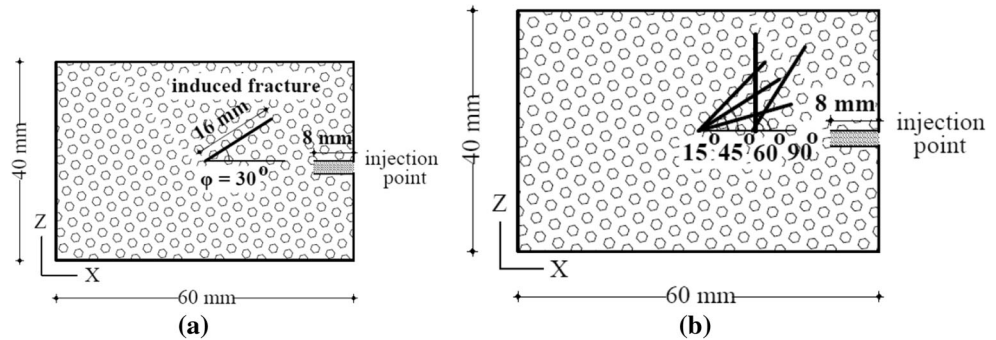
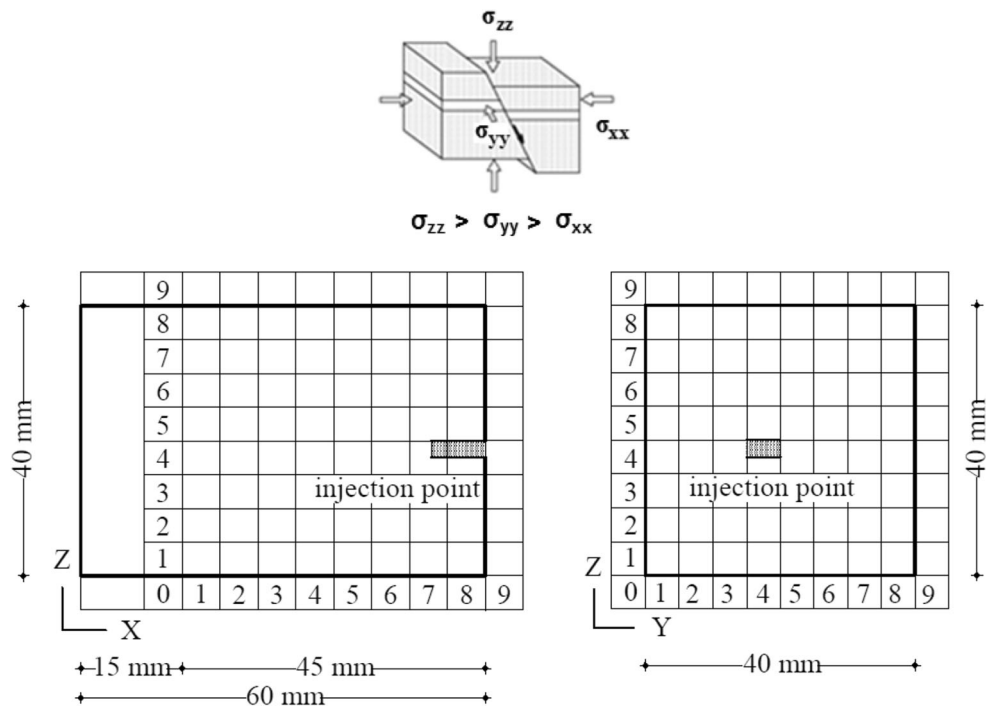


Fig. 8 Top example of an actual stress regime, and bottom fluid cell grid in the zx and zy planes



size and an induced inclined fracture 15 mm long at angle increments of 15° up to 90° (Fig. 7a). The fractures were created by deleting the particles and their bonds that were included in the relevant region of the fracture. The combination between the overall dimensions and the particle’s size determined the design of the model. More specifically, the angle 15° was the smallest distinguishable angle for the particular particle size of the model. The test was repeated five times for each different inclined fractures (Fig. 7b). For brevity, the samples for the simulated fluid test are named LIM1_15° to _90° and the fluid injection well was replicated at the centre of the right-hand side of the model.

A fluid-coupling algorithm, based on the Navier–Stokes equations for porous media, was used for this investigation as a function that has already been developed by the Itasca-Consulting-Group (2008c). The fluid-flow logic can be considered as a two-way coupling as the fluid injection has altered the structure of the rock (in terms of particle movement and fractures at the microlevel) and the fracturing has also altered the path of the fluid flow.

The aim of the test was to investigate the injection of a steady fluid flow into one end of a virtual rock sample, thus simulating an on-site horizontal injection well, and the creation of a pressure built up until the internal stress state of the assembly was tense enough to initiate microcracks which will interact with the existing fractures. The progress of the fracture propagation was monitored in terms of broken parallel bonds under the influence of the fluid. The breakage of the bonds was recorded as either tensile or shear cracks with respect to the bond plane. The virtual sample was enclosed within solid boundary walls in order to replicate the actual conditions, where underground rocks are naturally pressurized from the surroundings for reasons such as the depth of overburden, the interactions between tectonic plates or the topography in general. The walls are

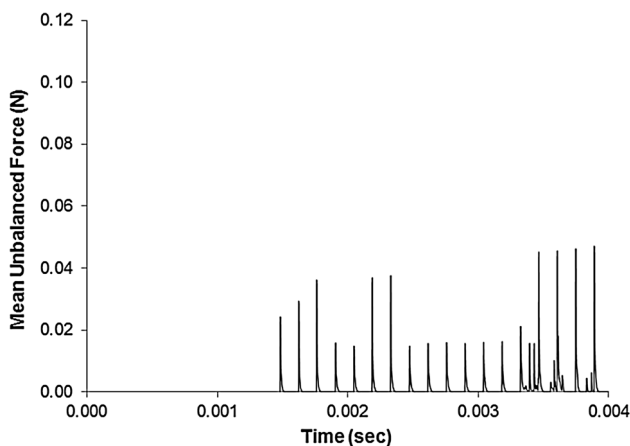


Fig. 9 Progress of the mean unbalanced force at each pressure increase versus time for the LIM1 assembly. The force reaches a peak value and then drops to zero reaching equilibrium

continuously moving in order to apply a constant confinement simulating an example of an actual stress regime (Fig. 8, top). The stress in the z direction (vertical) was the principal stress ($\sigma_{zz} = 1.5$ MPa) followed by the stress in the x direction ($\sigma_{xx} = 1$ MPa) (same as the direction of the fluid) and the stress in the y direction ($\sigma_{yy} = 0.5$ MPa).

Next a fluid cell grid was applied to perform the fluid analysis. Only a part of the sample was surrounded by the fluid cells (45 × 40 × 40 mm), leaving enough space for the fluid to exit and still be within the rock (Fig. 8, bottom). The purpose of the *partial* fluid grid was to replicate and comply with reality as close as possible, where the output of the fluid will still be inside the formation. The parameters defining the grid were its dimensions and the number of cells along each direction. There are no guidelines on the grid parameters, other than in the case of a porous medium consisting of small particles, each cell should have a size comparable to that of a few particle diameters. This is due to the fact that the porosity and the permeability are calculated through each cell, thus the cell grid must be coarse.

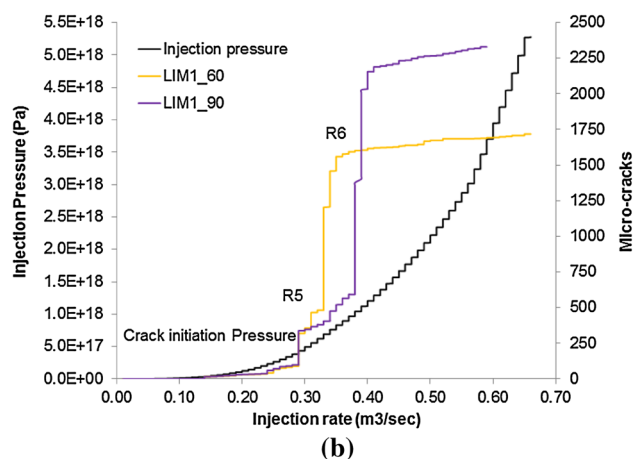
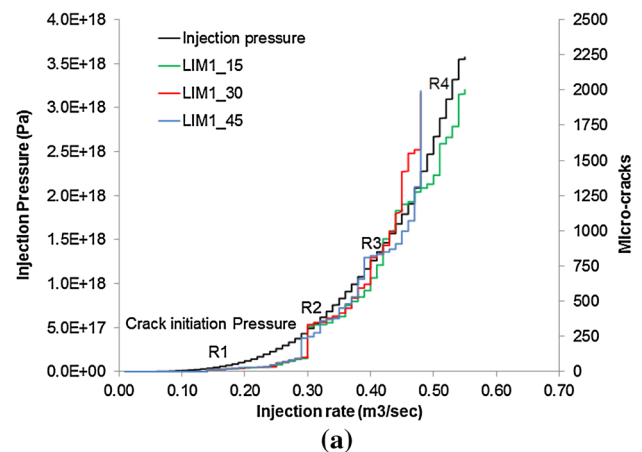


Fig. 10 Injection pressure and total number of microcracks versus the flow rate for **a** the LIM1_15°, LIM1_30° and LIM1_45°, and **b** the LIM1_60° and LIM1_90° samples

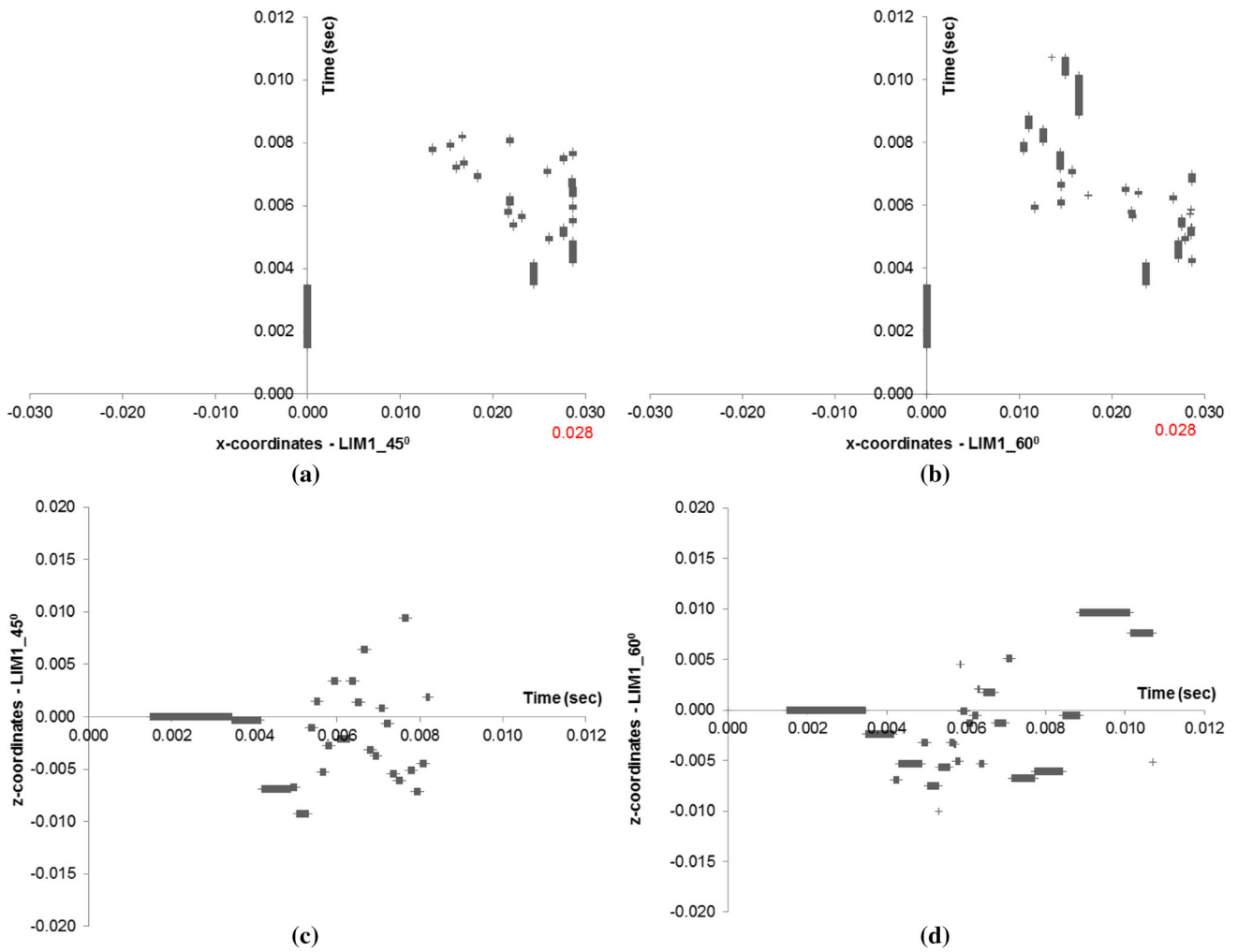


Fig. 11 Coordinates of microcracks in the x directions for **a** the LIM1_45° and **b** the LIM1_60° samples and in the z directions for **c** the LIM1_45° and **d** the LIM1_60° samples versus time

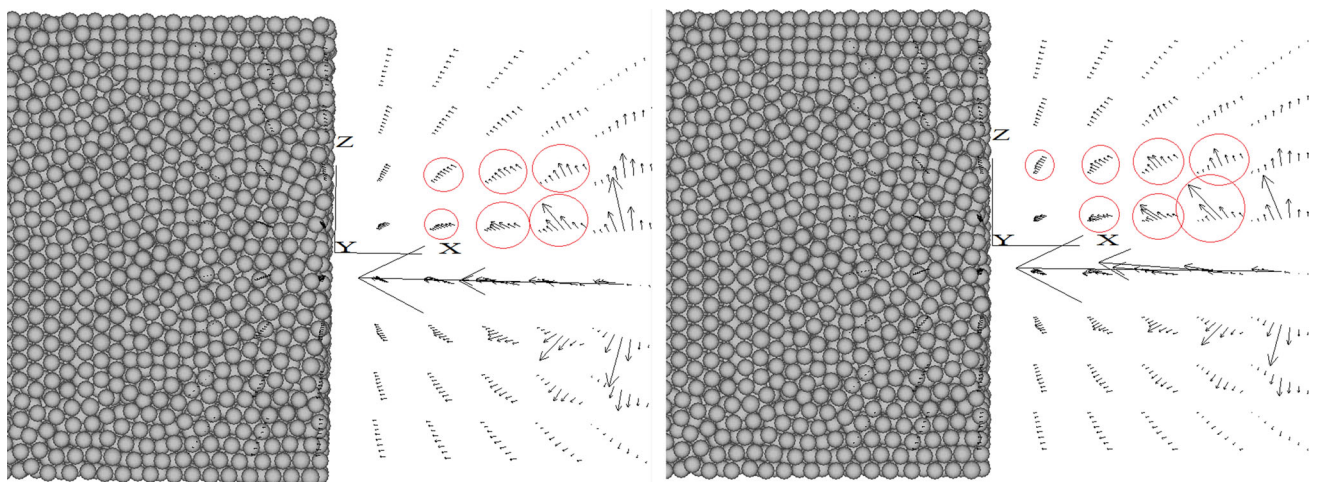


Fig. 12 Side view of one half of the virtual assembly. The fluid velocity vectors in the upper part of the assembly for the LIM1_30° (*left*) and the LIM1_60° (*right*) samples, respectively

The size of the cells was considered based on the allowable volume of particles so that the results will not be sensitive to the size, and therefore 1,000 cells were created, each with a cell size of $5.625 \times 5.0 \times 5.0$ mm. The simulated fluid was water with a density and viscosity of $1,000 \text{ kg/m}^3$ and 10^{-3} Pa s , respectively.

The injection was invoked through a single cell (centre right-hand-side of the fluid cell grid) with an initial rate of $9 \times 10^{-6} \text{ m}^3/\text{s}$, and it was gradually increased with a gradient of $1 \times 10^{-2} \text{ m}^3/\text{s}$, in order to accelerate the process of crack propagation. A preliminary study showed that in order for the test to be performed within a reasonable timeframe, a gradient within the range of 10^{-2} to 10^{-3} had to be applied with no significant difference between the boundary values. Furthermore, convergence tests showed that even though a relatively high gradient was used, the

overall mechanical response on the virtual assembly was not significantly affected in order to compromise the results. The injection rate at the end of the test was measured to be between 0.55 and $0.66 \text{ m}^3/\text{s}$ for all sample types. A number of preliminary tests diagnosed the state of the model at the end of each rate change. It was concluded that 3,000 mechanical cycles were sufficient for the pressure disturbance to be transmitted throughout the sample. During these tests, the algebraic sum of the forces acting between the particles and walls was almost zero, meaning that the forces acting on each particle were almost in balance. Figure 9 illustrates the mean unbalanced force versus time, where abrupt jumps are recorded due to the rate gradient reaching zero after 3,000 cycles.

Finally, when the microcracks reached the hollow core of the inclined fracture, the test was terminated.

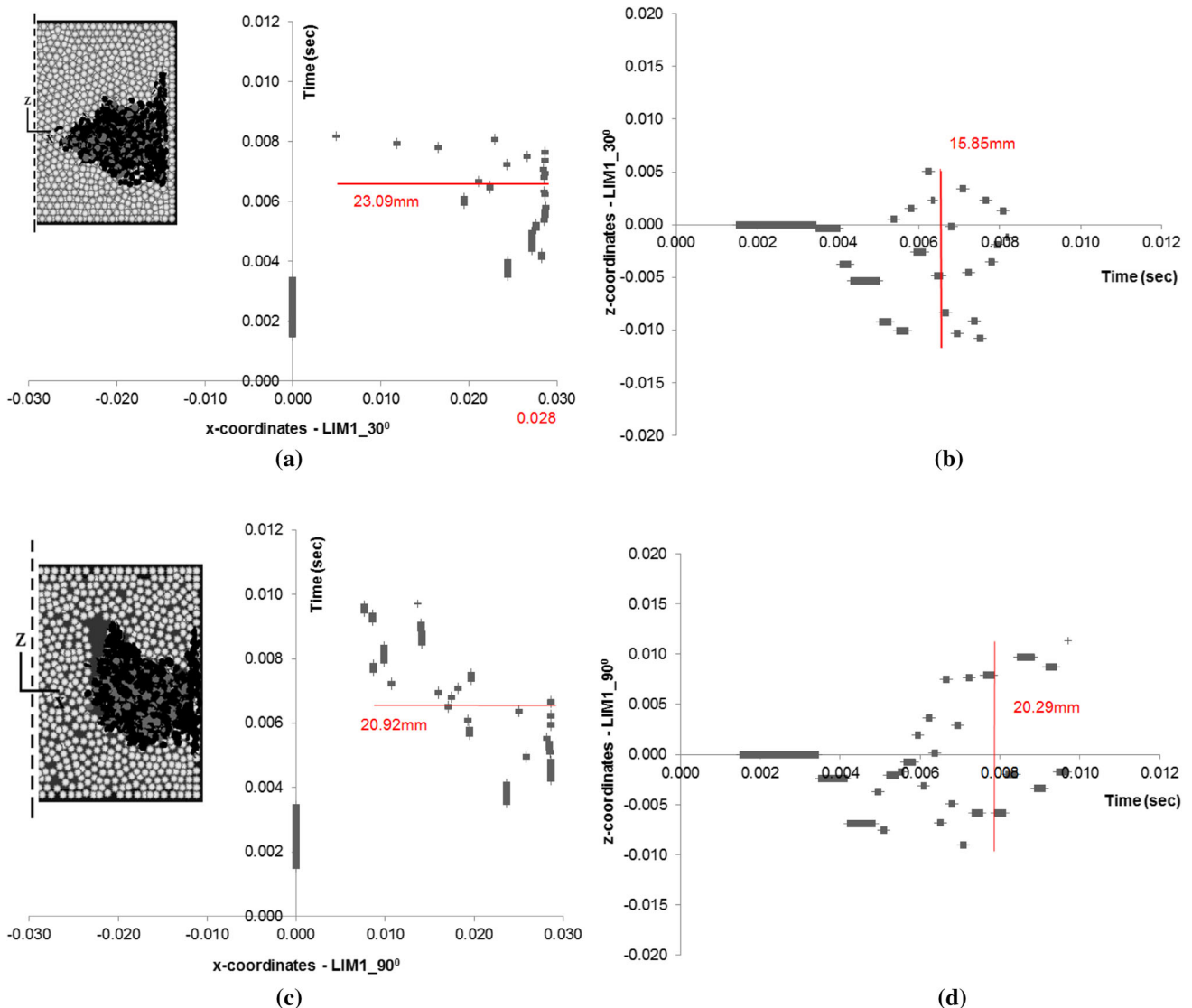


Fig. 13 Coordinates of microcracks and the overall fracture growth in the x directions for **a** the LIM1_30° and **b** the LIM1_90° samples and in the z directions for **c** the LIM1_30° and **d** the LIM1_90° samples versus time

Preliminary tests showed that 2,000 microcracks were considered enough in terms of propagation in order to be sufficiently far from the injection point and reach the inclined fracture.

Results and discussion

Figure 10a, b illustrates the resulting injection pressure versus the injection rate for the LIM1_15°, LIM1_30°, LIM1_45°, LIM1_60° and LIM1_90° samples, respectively, as well as the total number of microcracks until the termination of the test. It can be observed that the cracks start to generate at around 3×10^{16} Pa pressure for all cases, a reasonable outcome since the reference point is almost the same for all samples (right-hand side of inclined fracture see Fig. 7b). However, it is interesting to note that the pressure that corresponds to the 2,000 microcracks and the end of the test (namely P_b) is being reduced for fractures below 45° taking a maximum value of about 3.57×10^{18} Pa when the angle is 15°. The reversed behaviour has been observed for angles 45° and upwards, marking the 45° a critical one. The additional injection required for shallow angles can be attributed to the fact that the low angle is close to zero and thus can be considered horizontal, in opposition to the horizontal fluid movement.

The observed high injection pressures during the investigation act only as a medium to facilitate fracturing in a hydraulic manner, and are not applicable in real applications, although it is not uncommon for similar studies (Martinez 2012). Moreover, the aim of this work is to study the generation and microcracking patterns of a rock assembly and not to draw conclusions on the injection pressure values for real-world applications. Given the available resources, the sample dimensions, simulation time and injection pressure gradients were selected appropriately so as to lead to a feasible model in terms of simulation time. A preliminary study showed that in order for the test to be performed within a reasonable timeframe, a gradient within the range of 10^{-2} to 10^{-3} had to be applied with no significant difference between the boundary values. Furthermore, convergence tests showed that even though a relatively high gradient was used, the overall mechanical response on the virtual assembly was not significantly affected in order to compromise the results.

Furthermore, it can be observed that there are regions with sudden increase of cracks (R1–R6) indicating brittle material behaviour in terms of crack generation/propagation. More specifically, for angles above the 45°, the material demonstrates more aggressive behaviour in terms of fracking (Fig. 10b) as soon as the fluid reaches the hollow zone within the fracture. This boosts the fluid velocity resulting in cumulating fracking.

Figure 11 demonstrates the coordinates in the horizontal x and vertical z directions during the simulation for the LIM1_45° and 60° samples. It can be observed that for the LIM1_45°, the cracks initiate near the injection point ($x = 28$ mm, marked with red) following horizontal (towards the diagonal fracture) and a slight downwards expansion after the second half of the simulated time (after 0.006 s). The movement towards the negative part of the z axis can be attributed to the influence of gravity which, even though it may be considered a minor effect on the macro-scale, affects the behaviour of the virtual assembly in this particle scale. The same behaviour was recorded for angles 15° and 30°, respectively, which are not presented for the sake of brevity. The preferred direction of the cracks' propagation for the LIM1_60° was dissimilar. More specifically, it required less injection for the sample to reach the diagonal fracture ($0.46 \text{ m}^3/\text{s}$ for the LIM1_45° compared to $0.31 \text{ m}^3/\text{s}$ for the LIM1_60°) and the horizontal cracks propagated further, reaching about $x = 10$ mm (compared to 14 mm for the LIM1_45°), while the downwards expansion has been slowed down. More cracks tend to develop towards the positive part of the z axis (upwards) in the second half of the simulated test. Considering the abrupt increase in Fig. 10b, which occurs in the second part of the simulated test, it appears to enhance the fluid movement of the fractures above 45°, and therefore the propagation of cracks towards their relevant plane.

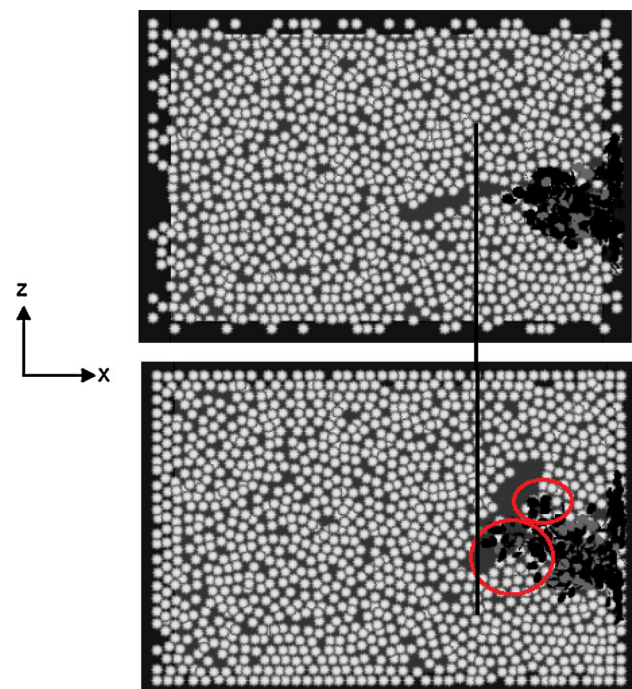


Fig. 14 Schematic of the cross sections for the LIM1_15° (top) and the LIM1_60° (bottom) samples, respectively, illustrating the locations of the microcracks and the groups of cracks (red circles) that stray from the main volume

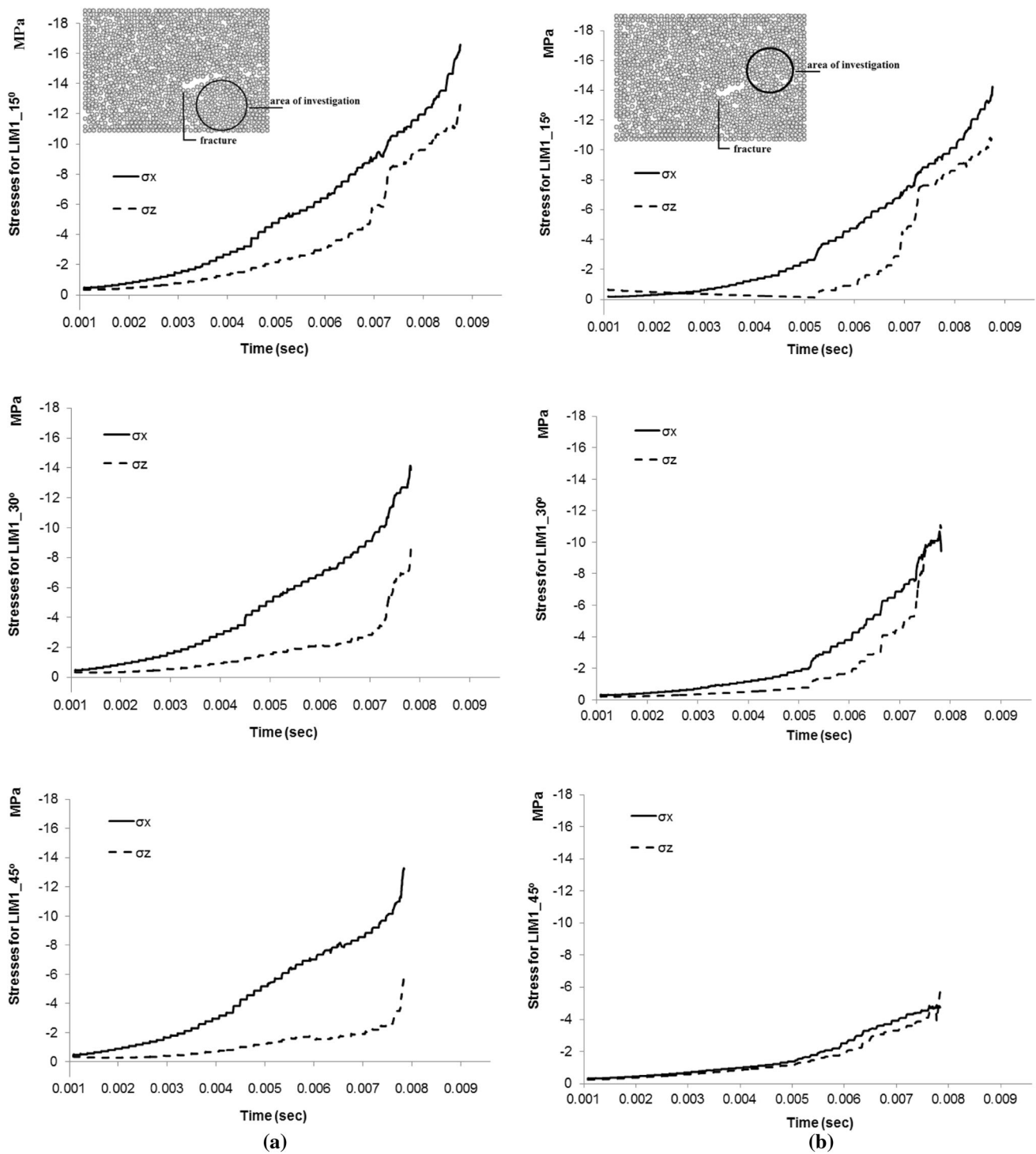


Fig. 15 Stresses in the x and z directions versus time for the LIM1_15°, 30°, 45° samples, respectively, in **a** the lower part of the diagonal fracture, and **b** the upper part of the diagonal fracture

The aforementioned postulate can also be observed from the fluid vectors shown in Fig. 12 which compares the samples LIM1_30° and LIM1_60°, respectively. All the samples containing a diagonal fracture below 45° have similar behaviour in terms of fluid velocity vectors, and

they can be described by Fig. 12 (left). The velocity vectors between the upper and lower parts of the z axis appear to be almost the same, thus verifying the symmetrical and slightly downward propagation of cracks for the LIM1_45°. Moreover, the velocity vectors for the

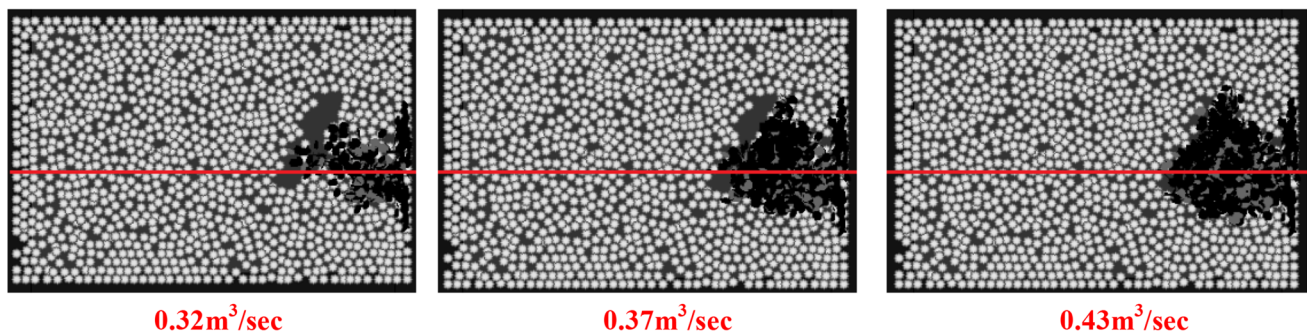


Fig. 16 Propagation of the cracks for the LIM1_60° sample after the second half of the simulated test. The red line indicates the height of the injection point

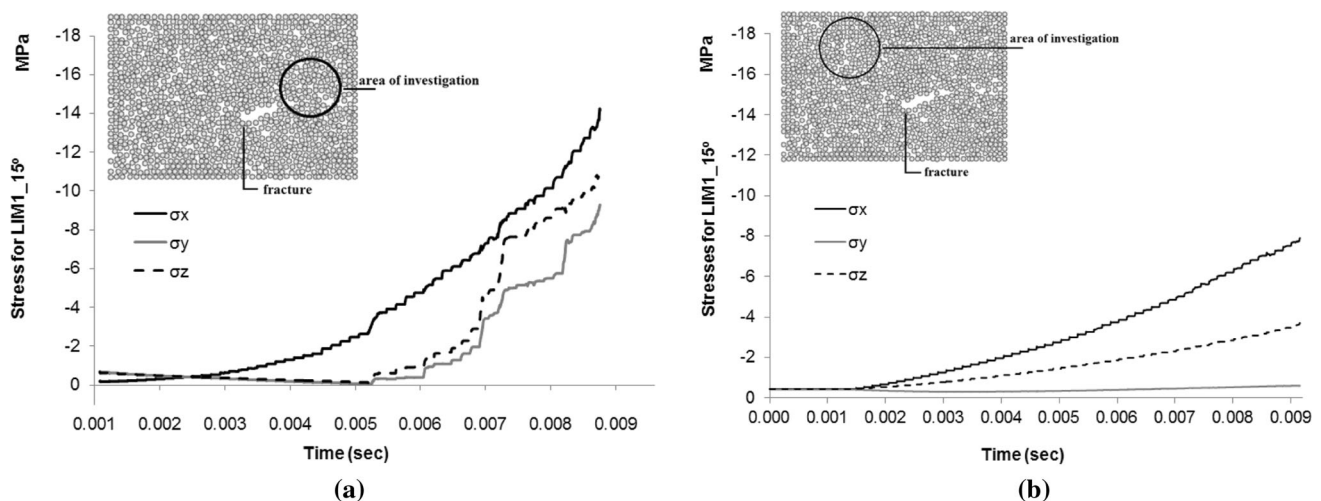


Fig. 17 Stresses versus time for the LIM1_15° sample **a** in front of the fracture tip, and **b** at a remote location away of the fracture

LIM1_60° sample are sufficiently larger in the upper part of the assembly, thereby indicating that the fluid tends to travel further in the upper part rather than the lower part.

The boundary conditions for this test were based on the assumption that the external stress regime was normal, and thus the vertical stress (σ_{zz}) was considered the principal compressive stress. However, the mechanical load altered the stress pattern, due to the high amount of injection pressure, making the horizontal stress (σ_{xx}) the maximum compressive stress throughout the model. Moreover, the propagation of the microcracks has been extended considerably in the horizontal and vertical directions, looking from the microscopic point of view, with the horizontal expansion gaining ground. Figure 13a, b is a representative example, where the overall growth in the horizontal direction for the LIM1_30° sample is larger than the one in the vertical direction. Even though the difference between the horizontal and vertical overall expansions is not always noticeable (Fig. 13c, d), from a macroscopic point of view, we can claim that the overall fracture growth in terms of a large rock extends along the principal compressive stress, agreeing with the conventional theory (Valko and

Economides 1995). The differences between the conventional theory and the microscopic observations of the hydraulic fracture growth can be attributed to the fact that the PFC sample is not homogeneous due to fractures and discontinuities.

Furthermore, as shown in Fig. 14 (bottom), regions of groups of microcracks appear to stray from the main volume of the cracks and form individual strands that can enhance the hydraulic conductivity. It can be observed that more cracks tend to separate from the main volume, propagating further ahead and upwards when the fracture is at 60°, whereas for lower angles, the cracks tend to develop in the lower part of the assembly and propagate as a cluster. The microcracks in the normal direction (black dots) are dominant, with a percentage of around 83 %, whereas only 17 % are formed in the shear direction (grey dots). This is an expected outcome since the ratio between the bonds' strength in the normal to shear direction is less than 1.

Measurements of the stresses in the horizontal (σ_x) and vertical (σ_z) directions for all samples provide a further understanding of the fracturing process and the influence of

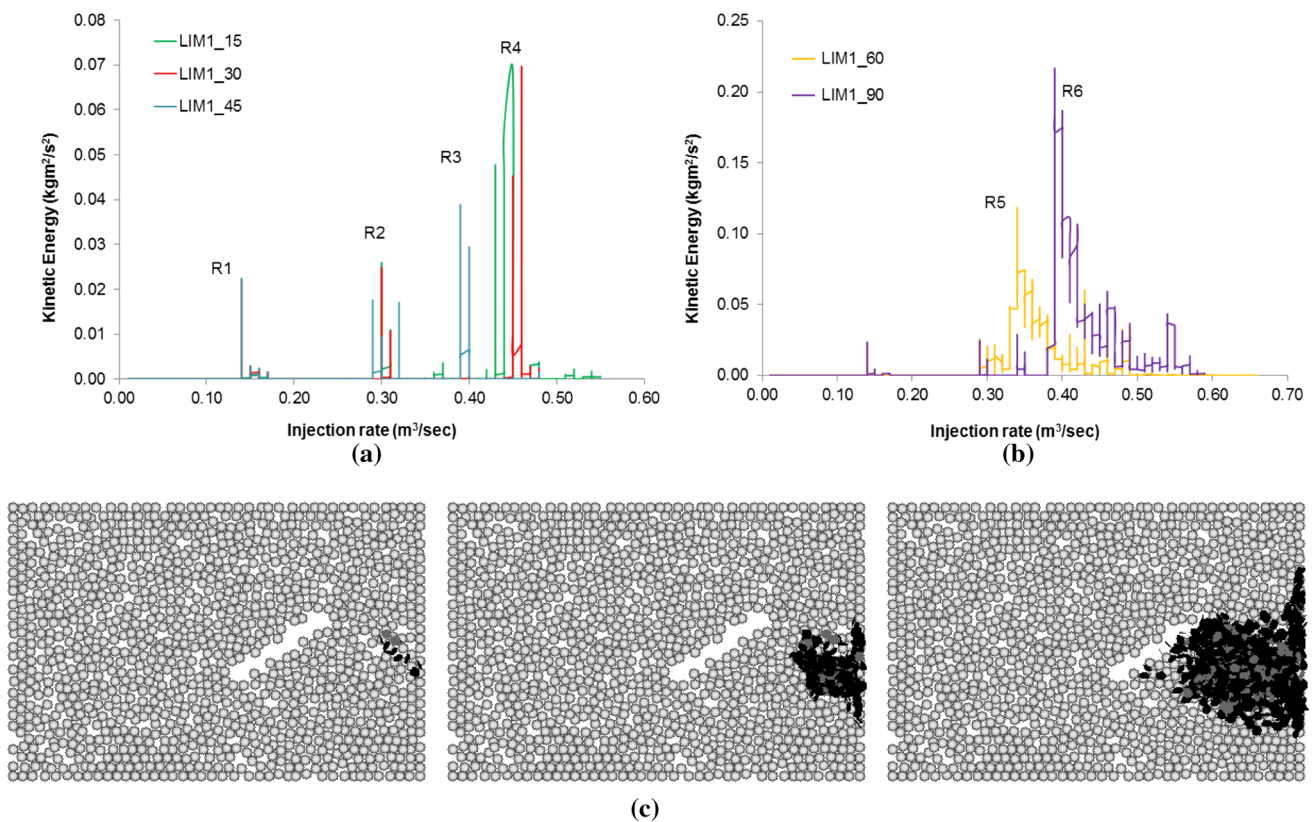


Fig. 18 Critical regions of energy release versus the injection rate for **a** the LIM1_15°, LIM1_30°, LIM1_45° and **b** the LIM1_60°, LIM1_90° samples, respectively, and **c** regions R2, R3, R4 of the

LIM1_30° sample showing the corresponding damage of the sample, relating the results with Fig. 10a

the fracture angle of the virtual assembly. More specifically, as shown in Fig. 15, the stresses in the areas below the diagonal fracture (Fig. 15a) for the samples with fractures between 15° and 45° are higher than those in the upper part of the fracture (Fig. 15b) and thus confirms the preferred propagation of cracks towards the negative part of the z axis.

The opposite behaviours, in terms of the overall stress in the lower and upper parts of the fracture, has been observed for the LIM1_60° and LIM1_90° samples; however, for brevity, only the results from the first set of angles are presented. The description of the previous conclusion can be observed in Fig. 16, where each microcracking corresponds to 0.32, 0.37 and 0.43 m³/s injection rates, respectively. The red line demonstrates the height of the injection point, while the hollow region is the fracture at 60°. It can be observed that cracks propagate more towards the upper part of the assembly and that, the breakage of the bonds, which connect the particles next to the fracture, results in an abrupt increase in the number of cracks. This explains the boost in fluid velocity, and this agrees with the results presented in Fig. 10b.

Previous research has established that the amounts of elastic energy which is stored within the virtual assembly in

the form of bond, friction, kinetic, strain and body energy are released every time a bond breaks. The extra pressure at each time-step, and hence the higher stresses, causes a greater energy release during the rupture of the bonds, especially near the fracture tip, thereby forcing the cracks to propagate to the next neighbouring location. This can be observed in Fig. 17, which illustrates the stresses in all directions for the regions near the right-hand side of the diagonal fracture tip and at another point away from the fracture (top and left-end of the assembly—Fig. 17b). It can be observed that the stresses near the tip are much higher (Fig. 17a) than those in the remote locations (Fig. 17b).

Moreover, Fig. 18a, b illustrates the changes in the stored energy, indicating that in the critical regions R1–R6, abrupt microcracks increases are followed by sudden and large increases in the kinetic energy within the assembly. The LIM1_15°, 30°, and 45° samples demonstrate a similar behaviour, whereas for the LIM1_60° and 90° samples, the kinetic energy shows concentrated high values in a time period near the second part of the simulated test. This is due to the enhanced fluid movement as it reached the hollow region within the fracture as previously discussed. Furthermore, the regions R1, R2 and R4 of the LIM1_30° cross sections can be seen in Fig. 18. One can observe the

progressive and sudden increase of the microcracks due to high hydraulic pressure and their propagation towards the hollow region of the fracture. The three pictures correspond in the relevant injection rates of 0.15, 0.30 and 0.45 m³/s from left to right followed by 15, 335 and 1,424 microcracks respectively. Similar behaviour has been observed for all samples.

Conclusions

The objectives of this paper are the computational modelling of a hydraulic fracturing test for a naturally fractured limestone sample, the analysis of its mechanical behaviour and the interaction between the natural fractures and the new hydraulic fractures. A parametric study of the angles of the induced fracture attempts to shed more light on how a fractured rock can influence and possibly enhance the fracking process. A series of Uniaxial, Brazilian and Single Edge Notch Bending tests were also included in order to validate the DEM model by comparing the simulated tests results from the calibration process to those obtained from the literature.

This paper has analysed the mechanical response of the rock model due to fluid flow by using the fluid-coupled DEM code in a number of hydraulic fracturing simulations. It involved detailed monitoring of the initiation/propagation of microcracks, analysis of the stresses in different regions within the rock's matrix and evaluation of the relation between the energy release and the development of cracks. Before moving to the hydraulic fracturing process, five DEM models were created and found to be well within the wide range of limestone characteristics, while the results from the simulated SENB test were found to be in excellent agreement with the previously reported experimental work.

The hydraulic fracturing test was performed in one of the DEM models and was repeated five times following the different angles of the natural fracture. Observations of the simulated tests showed that the angle of the fracture directly relates with the stress pattern within the model, thus affecting the direction and propagation of cracks. It can be concluded that for angles below 45°, the stress regime below the fracture is always higher than the one in the upper part of the model and thus the cracks tend to propagate downwards and travelling mostly as a group of cracks. In contrast, for angles above 45°, there is the opposite stress regime and thus results in the easier upwards movement of the cracks forming clusters that stray from the main volume of cracks. The fracture is mainly observed towards the horizontal x axis, namely, along the direction of the maximum compressive principal stress, and this is in agreement with the conventional theory. Although this effect is pronounced, its magnitude in

the simulations is restricted by the sample dimensions and the need for computational time efficiency. Finally, it is observed that there is a clear relation between the important cracking events (large increases of microcracks) in each model with the energy release within the models. This validates the claim that bond breakage causes further movement of particles and therefore increases the internal kinetic energy.

Modelling of this nature, where natural fractured rocks are submitted into hydraulic fracturing, are in an early stage. and therefore this study attempts to provide further insights. This work can be a valuable outcome for EOR and/or EGR applications since it can contribute further understanding towards a safer reservoir productivity.

Acknowledgments The lead author, Sousani Marina, would like to thank the School of Civil Engineering and the Energy Technology and Innovation Initiative (ETII) of the School of Process, Environmental and Materials Engineering, University of Leeds for sponsoring this research.

References

- Adachi J, Siebrits E, Peirce A, Desroches J (2007) Computer simulation of hydraulic fractures. *Int J Rock Mech Min Sci* 44:739–757
- Anderson TL (1991) Fracture mechanics: fundamentals and applications, 3rd edn. CRC Press, Boca Raton
- Assane Oumarou T, Cottrell BE, Grasselli G (2009) Contribution of surface roughness on the shear strength of indiana limestone cracks—an experimental study. In: *Rock joints and jointed rock masses*, Tucson
- ASTM I (2001) Standard test method for measurement of fracture toughness. ASTM I, West Conshohocken
- Chen S, Doolen GD (1998) Lattice Boltzmann method for fluid flows. *Annu Rev Fluid Mech* 30:329–364
- Deng S, Li H, Ma G, Huang H, Li X (2014) Simulation of shale–proppant interaction in hydraulic fracturing by the discrete element method. *Int J Rock Mech Min Sci* 70:219–228
- Dong S (2007) Direct numerical simulation of turbulent Taylor–Couette flow. *J Fluid Mech* 587:373–393
- Economides MJ, Martin T (2007) Modern fracturing—enhancing natural gas production. BJ Services Company, Houston
- Economides MJ, Nolte KG (2000) Reservoir stimulation. Wiley, West Sussex
- Eshiet KI, Sheng Y (2010) Modelling erosion control in oil production wells world academy of science. *Eng Technol* 70:2093–2101
- Eshiet K, Sheng Y (2014a) Investigation of geomechanical responses of reservoirs induced by carbon dioxide storage. *Environ Earth Sci* 71:3999–4020. doi:10.1007/s12665-013-2784-2
- Eshiet K, II, Sheng Y (2014b) Carbon dioxide injection and associated hydraulic fracturing of reservoir formations. *Environ Earth Sci* 72:1011–1024
- Eshiet KI, Sheng Y, Jianqiao Y (2013) Microscopic modelling of the hydraulic fracturing process. *Environ Earth Sci* 68:1169–1186. doi:10.1007/s12665-012-1818-5
- Griffith AA (1921) The Phenomena of Rupture and Flow in Solids *Philosophical Transactions of the Royal Society of London Series A, Containing Papers of a Mathematical or Physical Character* 221:163–198 doi:10.1098/rsta.1921.0006

- Haimson BC (2004) Hydraulic fracturing and rock characterization. *Int J Rock Mech Min Sci* 41(Suppl 1):188–194
- Hallsworth CR, Knox RWO'B (1999) British Geological Survey: classification of sediments and sedimentary rocks. vol 3. British Geological Survey, Nottingham
- Hamidi F, Mortazavi A (2014) A new three dimensional approach to numerically model hydraulic fracturing process. *J Pet Sci Eng*. doi:10.1016/j.petrol.2013.12.006
- Huang H, Lecampion B, Detournay E (2013) Discrete element modeling of tool-rock interaction I: rock cutting. *Int J Numer Anal Meth Geomech* 37:1913–1929. doi:10.1002/nag.2113
- Huang Y, Zhou Z, Wang J, Dou Z (2014) Simulation of groundwater flow in fractured rocks using a coupled model based on the method of domain decomposition. *Environ Earth Sci* 72:2765–2777
- Itasca-Consulting-Group (2008a) Example's application 9: incorporation of fluid coupling in PFC3D, 4th edn. ICG, Minneapolis
- Itasca-Consulting-Group (2008b) FISH in PFC3D 3: PFC FishTank, 4th edn. ICG, Minneapolis
- Itasca-Consulting-Group (2008c) Particle flow code in 3 dimensions (PFC3D), 4th edn. ICG, Minneapolis
- Itasca-Consulting-Group (2008d) Theory and background 1: general formulation, 4th edn. ICG, Minneapolis
- Kasza P, Wilk K (2012) Completion of shale gas formations by hydraulic fracturing. *Przem Chem* 91:608–612
- Knill JL, Cratchley CR, Early KR, Gallois RW, Humphreys JD, Newbery J, Price DG, Thurrell RG (1970) The logging of rock cores for engineering purposes. vol 3. Geological Society Engineering Group Working Party Report
- Krajcinovic D (2000) Damage mechanics: accomplishments, trends and needs. *Int J Solids Struct* 37:267–277
- Martinez D (2012) Fundamental hydraulic fracturing concepts for poorly consolidated formations. University of Oklahoma, Oklahoma
- Mas Ivars D, Pierce ME, Darcel C, Reyes-Montes J, Potyondy DO, Paul Young R, Cundall PA (2011) The synthetic rock mass approach for jointed rock mass modelling. *Int J Rock Mech Mining Sci* 48:219–244
- Moin P, Mahesh K (1998) Direct numerical simulation: a tool in turbulence research. *Annu Rev Fluid Mech* 30:539–578
- Moon T, Nakagawa M, Berger J (2007) Measurement of fracture toughness using the distinct element method. *Int J Rock Mech Min Sci* 44:449–456
- Nagel N, Gil I, Sanchez-nagel M, Damjanac B (2011) Simulating hydraulic fracturing in real fractured rocks, SPE Hydraulic Fracturing Technology Conference, 24–26 Jan, The Woodlands, Texas, USA
- Potyondy DO, Cundall PA (2004) A bonded-particle model for rock. *Int J Rock Mech Mining Sci* 41:1329–1364
- Rahm D (2011) Regulating hydraulic fracturing in shale gas plays: The case of Texas. *Energy Policy* 39:2974–2981
- Schlangen E, Garboczi EJ (1997) Fracture simulations of concrete using lattice models: computational aspects. *Eng Fract Mech* 57:319–332
- Schmidt R (1976) Fracture-toughness testing of limestone. *Exp Mech* 16:161–167. doi:10.1007/bf02327993
- Schmidt RA, Huddle CW (1977) Effect of confining pressure on fracture toughness of Indiana limestone. *Int J Rock Mech Mining Sci Geomech Abstracts* 14:289–293
- Shimizu H, Murata S, Ishida T (2011) The distinct element analysis for hydraulic fracturing in hard rock considering fluid viscosity and particle size distribution. *Int J Rock Mech Min Sci* 48:712–727
- Sousani M, Eshiet KI-I, Ingham D, Pourkashanian M, Sheng Y (2014) Modelling of hydraulic fracturing process by coupled discrete element and fluid dynamic methods. *Environ Earth Sci*. doi:10.1007/s12665-014-3244-3
- Tran Ngoc TD, Lefebvre R, Konstantinovskaya E, Malo M (2014) Characterization of deep saline aquifers in the Bécancour area, St. Lawrence Lowlands, Québec, Canada: implications for CO₂ geological storage *Environ Earth Sci* 72:119–146
- University-of-Stanford Some Useful Numbers on the Engineering Properties of Materials. <http://www.stanford.edu/~tyzhu/Documents/Some%20Useful%20Numbers.pdf>. Accessed September 2013
- Valko P, Economides MJ (1995) Hydraulic fracture mechanics. Wiley, Chichester
- Wang H, Wang E, Tian K (2004) A model coupling discrete and continuum fracture domains for groundwater flow in fractured media. *J Hydraul Res* 42:45–52
- Weng X, Kresse O, Cohen C-E, Wu R, Gu H (2011) Modeling of hydraulic-fracture-network propagation in a naturally fractured formation. *Soc Pet Eng* 26(4):368–380
- Wu Q, Liu Y, Liu D, Zhou W (2011) Prediction of floor water inrush: the application of gis-based AHP vulnerable index method to donghuantuo coal mine. *China Rock Mech Rock Eng* 44:591–600
- Hertzberg RW (1996) Deformation and fracture mechanics of engineering materials, 4th edn. Wiley, New York
- Zhu B, Wu Q, Yang J, Cui T (2014) Study of pore pressure change during mining and its application on water inrush prevention: a numerical simulation case in Zhaogezhuang coalmine. *China Environ Earth Sci* 71:2115–2132